Saturation of intersubband transitions in *p*-type semiconductor quantum wells

Yia-Chung Chang
Department of Physics and Materials Research Laboratory, University of Illinois at Urbana-Champaign, Urbana, Illinois 61801

R. B. James
Theoretical Division, Sandia National Laboratories, P.O. Box 969, Livermore, California 94550

(Received 21 December 1988)

Saturation behavior of intersubband optical transitions in *p*-type semiconductor quantum wells is examined theoretically with the multiband effective-mass model. Carrier-phonon scatterings are taken into account within the deformation-potential approximation. Deviation of the hole distribution from thermal equilibrium due to optical pumping is calculated by solving coupled rate equations. Pump-and-probe absorption spectra are also studied, and possible applications for light-by-light modulation are discussed.

I. INTRODUCTION

Photoabsorption in *p*-type semiconductor quantum wells at photon wavelengths near 10 μm is dominated by direct optical transitions between the partially filled subbands near the valence-band maximum and the unfilled higher subbands. The mechanism is similar to the intervalence-band transitions in several bulk *p*-type semiconductors in which direct free-carrier transitions between the heavy-hole and light-hole bands are allowed.[1] Theoretical calculations on intersubband transitions in *n*-type quantum wells have previously been reported.[2,3] The intersubband transitions in *p*-type quantum wells are more complicated than those in *n*-type quantum wells because of the mixing of heavy- and light-hole states[4–6] due to the quantum-well potential. The band-mixing effect has played an essential role in interpreting the $\Delta n \neq 0$ (n is the principal quantum number of quantum-well states) forbidden transitions commonly observed in the interband absorption spectra of quantum wells.[4,6,7]

At high intensities of the incident radiation, the carriers in the initial states tend to be depleted by optical pumping, and a saturation phenomenon of the absorption coefficient occurs.[8,9] This saturation property has application in nonlinear-optical devices used to achieve passive mode locking of CO_2 lasers and interstage isolation of CO_2-laser amplifiers. For example, the saturable absorption of some *p*-type semiconductors such as Ge and GaAs have been utilized to generate passively mode-locked pulses of subnanosecond duration.[10–12] Semiconductor quantum wells provide a way for modifying the band structure and thereby tuning the saturation behavior to suit specific applications. Recently, many promising applications regarding the nonlinear-optical properties of semiconductor quantum wells have been reported.[13–15] In this paper we report theoretical studies of the linear and nonlinear absorption associated with intersubband transitions in *p*-type quantum wells. We find that the linear absorption spectrum due to intersubband transitions has a number of structures corresponding to transitions from the first few subbands (predominantly the first heavy-hole subband) to higher valence subbands.

II. PHOTOABSORPTION DUE TO INTERSUBBAND TRANSITIONS

To calculate the absorption due to intersubband transitions in *p*-type GaAs-$Al_xGa_{1-x}As$ quantum wells, we need a suitable description of the valence-band states. For *p*-type modulation-doped GaAs-$Al_xGa_{1-x}As$ quantum wells, the valence-subband structures can be well described by the multiband effective-mass theory.[6] According to the $\mathbf{k}\cdot\mathbf{p}$ theory, the valence-band structure of GaAs near the zone center can be obtained by diagonalizing a 4×4 Luttinger-Kohn Hamiltonian matrix $H^{(0)}(\mathbf{k})$.[16] $H^{(0)}(\mathbf{k})$ is defined in an orthonormal basis set $\{|u_{J\nu}\rangle\}$ of cell-periodic wave functions at $\mathbf{k}=\mathbf{0}$, where $J=\frac{3}{2}$ and $\nu=-\frac{3}{2},-\frac{1}{2},\frac{1}{2},\frac{3}{2}$ designate the total angular momentum and its z components, respectively.

Since a quantum well has translational invariance in the plane parallel to the interfaces, the in-plane wave vector $\mathbf{k}_\parallel$ is a good quantum number. A valence-subband state with wave vector $\mathbf{k}_\parallel$ can be expanded in terms of linear combinations of a set of basis states $\{|\nu,\mathbf{k}\rangle;\ \nu=-\frac{3}{2},-\frac{1}{2},\frac{1}{2},\frac{3}{2}\}$, which are the Bloch functions of bulk GaAs valence-band states correct to first order in the $\mathbf{k}\cdot\mathbf{p}$ perturbation,[1]

$$|\nu,\mathbf{k}\rangle = e^{i\mathbf{k}\cdot\mathbf{r}}\left[|u_{3/2,\nu}\rangle + \frac{\hbar}{m_0}\sum_s \frac{\langle u_s|\mathbf{k}\cdot\mathbf{p}|u_{3/2,\nu}\rangle}{E_0-E_s}|u_s\rangle\right], \quad (1)$$

where $|u_s\rangle$'s are cell-periodic functions at $\mathbf{k}=\mathbf{0}$ for all bands other than the four valence bands, E_s's are the corresponding zone-center energies, and E_0 is the energy of the valence-band maximum. The expansion for the quantum-well state $|n,\mathbf{k}_\parallel\rangle$ is written as

$$|n,\mathbf{k}_{\parallel}\rangle=\sum_{\nu,k_z} F_{\nu}(n\mathbf{k}_{\parallel},k_z)|\nu,\mathbf{k}\rangle \ , \tag{2}$$

where n is a label for the valence subbands, and $\mathbf{k}=\mathbf{k}_{\parallel}+k_z\hat{\mathbf{z}}$. Here we have chosen the growth direction to be along the z direction. $F_{\nu}(n\mathbf{k}_{\parallel},k_z)$ can be shown to satisfy the multiband effective-mass equation

$$\sum_{\nu'}[-H^{(0)}_{\nu,\nu'}(\mathbf{k}_{\parallel},k_z)-E_n(\mathbf{k}_{\parallel})\delta_{\nu,\nu'}]F_{\nu'}(n\mathbf{k}_{\parallel},k_z) + \sum_{k_z'}\langle k_z|V(z)|k_z'\rangle F_{\nu}(n\mathbf{k}_{\parallel},k_z')=0 \ , \tag{3}$$

where $V(z)$ is the quantum-well potential (including the modulation-doping effect) for the hole. We have ignored the mismatch between the valence-band parameters for GaAs and $Al_xGa_{1-x}As$. This is a good approximation as long as the holes are well confined in the quantum well. The valence-band discontinuity between GaAs and AlAs used in this paper is 450 meV.[17] The Fourier transform

$$F_{\nu}(n\mathbf{k}_{\parallel},z)\equiv\sum_{k_z}F_{\nu}(n\mathbf{k}_{\parallel},k_z)e^{ik_zz}$$

is called the envelope function of the quantum-well state.

A variational method was used to calculate the valence-band states.[6] Figure 1 shows the valence-subband structures of 80- and 50-Å GaAs-AlAs quantum wells. The optical properties of these quantum wells will be discussed extensively below. At the zone center ($\mathbf{k}_{\parallel}=\mathbf{0}$), the valence subbands are either heavy-hole (HH) -like or light-hole (LH) -like, and they are labeled HH1, LH1, HH2, HH3, etc., according to their characters and principal quantum numbers. For $\mathbf{k}_{\parallel}$ away from the zone center, heavy-hole and light-hole states are mixed; thus, we shall simply label them by the subband index n. The vertical arrows in the figure indicate the possible optical transitions for an incident photon energy of 0.117 eV.

The absorption coefficient for inter-valence-band transitions between subband n and subband n' is given by[9]

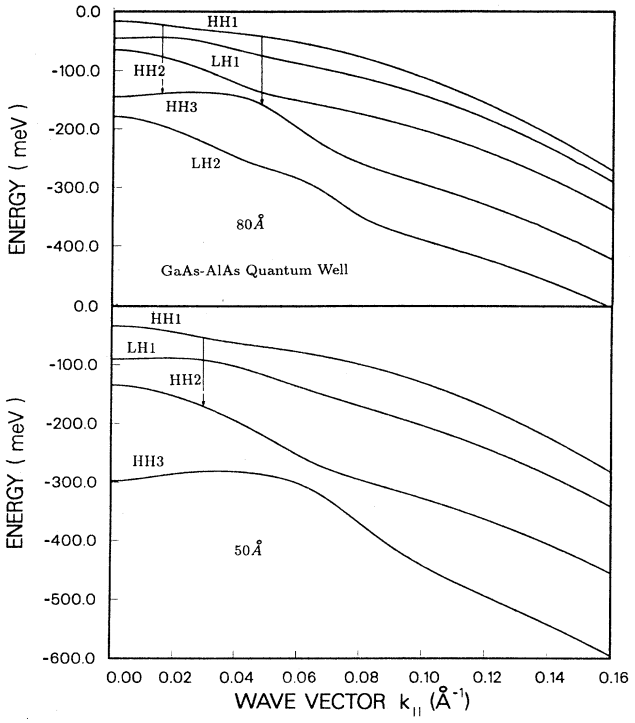

FIG. 1. Valence-subband structures of (a) 80-Å and (b) 50-Å GaAs-AlAs quantum wells.

$$\alpha_{nn'}(\omega)=\frac{4\pi^2e^2}{(\epsilon_1)^{1/2}m_0^2\omega c} \times\sum_{\mathbf{k}_{\parallel}}[f_n(\mathbf{k}_{\parallel})-f_{n'}(\mathbf{k}_{\parallel})]|\hat{\boldsymbol{\epsilon}}\cdot\mathbf{P}_{nn'}(\mathbf{k}_{\parallel})|^2 \times\frac{\hbar\Gamma_{nn'}(\mathbf{k}_{\parallel})/\pi}{[\Delta_{nn'}(\mathbf{k}_{\parallel})-\hbar\omega]^2+[\hbar\Gamma_{nn'}(\mathbf{k}_{\parallel})]^2} \ , \tag{4}$$

where ϵ_1 is the dielectric constant, m_0 is the free electron mass, $\Delta_{nn'}(\mathbf{k}_{\parallel})\equiv|E_{n'}(\mathbf{k}_{\parallel})-E_n(\mathbf{k}_{\parallel})|$, $E_n(\mathbf{k}_{\parallel})$ is the energy of subband n obtained by solving (3), $\mathbf{P}_{nn'}(\mathbf{k}_{\parallel})$ is the momen-

TABLE I. Coefficients defining the matrices $\hat{\boldsymbol{\epsilon}}\cdot\mathbf{P}$ and $\hat{\boldsymbol{\epsilon}}\cdot\mathbf{Q}$ according to (6).

$\hat{\boldsymbol{\epsilon}}\cdot\mathbf{P}$	$\hat{\boldsymbol{\epsilon}}\|\hat{\mathbf{x}}$	$\hat{\boldsymbol{\epsilon}}\|\hat{\mathbf{y}}$	$\hat{\boldsymbol{\epsilon}}\|\hat{\mathbf{z}}$
A_1	γ_1k_x	γ_1k_y	0
A_2	γ_2k_x	γ_2k_y	0
B	0	0	$-2\sqrt{3}\gamma_3(k_x-ik_y)$
C	$-2\sqrt{3}(\gamma_2k_x-i\gamma_3k_y)$	$2\sqrt{3}(\gamma_2k_y+i\gamma_3k_x)$	0
$\hat{\boldsymbol{\epsilon}}\cdot\mathbf{Q}$	$\hat{\boldsymbol{\epsilon}}\|\hat{\mathbf{x}}$	$\hat{\boldsymbol{\epsilon}}\|\hat{\mathbf{y}}$	$\hat{\boldsymbol{\epsilon}}\|\hat{\mathbf{z}}$
A_1	0	0	γ_1
A_2	0	0	γ_2
B	$-2\sqrt{3}\gamma_3$	$2\sqrt{3}i\gamma_3$	0
C	0	0	0

tum matrix element, $f_n(\mathbf{k}_\parallel)$ is the carrier distribution function associated with subband n, and $\Gamma_{nn'}(\mathbf{k}_\parallel)$ is the average scattering rate for the electronic states $|n,\mathbf{k}_\parallel\rangle$ and $|n',\mathbf{k}_\parallel\rangle$. The momentum matrix elements $\mathbf{P}_{nn'}(\mathbf{k}_\parallel)$ for the inter-valence-band transitions can be derived from the $\mathbf{k}\cdot\mathbf{p}$ theory.[1] The derivations are given in the Appendix. The final results are

$$\hat{\boldsymbol{\epsilon}}\cdot\mathbf{P}_{nn'}=\hbar\hat{\boldsymbol{\epsilon}}\cdot\sum_{\nu,\nu'}(\mathbf{P}_{\nu\nu'}O_{\nu\nu'}^{nn'}+\mathbf{Q}_{\nu\nu'}D_{\nu\nu'}^{nn'}) , \tag{5}$$

where $\hat{\boldsymbol{\epsilon}}\cdot\mathbf{P}_{\nu\nu'}$ and $\hat{\boldsymbol{\epsilon}}\cdot\mathbf{Q}_{\nu\nu'}$ are matrix elements of the 4×4 matrices $\hat{\boldsymbol{\epsilon}}\cdot\mathbf{P}$ and $\hat{\boldsymbol{\epsilon}}\cdot\mathbf{Q}$ written in the form

$$\begin{bmatrix} A_1+A_2 & B & C & 0 \\ B^* & A_1-A_2 & 0 & C \\ C^* & 0 & A_1-A_2 & -B \\ 0 & C^* & -B^* & A_1+A_2 \end{bmatrix} ,$$

with the coefficients A_1, A_2, B, and C given in Table I in terms of the Luttinger parameters $\gamma_1,\gamma_2,\gamma_3$, and wave-vector components k_x,k_y. $O_{\nu\nu'}^{nn'}$ and $D_{\nu\nu'}^{nn'}$ in (5) are elements of the overlap matrix $O^{nn'}$ and dipole matrix $D^{nn'}$, respectively. They are defined by

$$O_{\nu\nu'}^{nn'}=\int F_\nu^*(n\mathbf{k}_\parallel,z)F_{\nu'}(n'\mathbf{k}_\parallel,z)dz \tag{6}$$

and

$$D_{\nu\nu'}^{nn'}=i\int F_\nu^*(n\mathbf{k}_\parallel,z)\frac{\partial}{\partial z}F_{\nu'}(n'\mathbf{k}_\parallel,z)dz , \tag{7}$$

where $F_\nu(n\mathbf{k}_\parallel,z)$ is the envelope function associated with subband state $|n,\mathbf{k}_\parallel\rangle$.

Following the derivations given above, we can also obtain the momentum matrix elements for the intersubband transitions for n-type quantum wells. Dropping the index ν in the above formulations (since the conduction band is s-like, and the electron spinor can be factored out) we immediately obtain

$$\hat{\boldsymbol{\epsilon}}\cdot\mathbf{P}_{nn'}=\gamma_C(\epsilon_x k_x+\epsilon_y k_y)O^{nn'}+\gamma_C\epsilon_z D^{nn'} , \tag{8}$$

where $\gamma_C=m_0/m_C^*$ with m_C^* being the conduction-band effective mass. $O^{nn'}$ and $D^{nn'}$ are the overlap and dipole matrix elements for conduction-subband states similarly defined as in (6) and (7). Since two envelope functions associated with different principal quantum numbers (n and n') are orthogonal to each other, we have $O^{nn'}=0$ for $n\neq n'$. The results for n-type quantum wells are identical to those given in Ref. 3. A number of comments are in order at this point. First, we note that the matrix $\hat{\boldsymbol{\epsilon}}\cdot\mathbf{P}$ is linear in $\mathbf{k}_\parallel$, whereas the matrix $\hat{\boldsymbol{\epsilon}}\cdot\mathbf{Q}$ is independent of $\mathbf{k}_\parallel$. Second, the overlap matrix $O^{nn'}$ only couples envelope functions of the same parity, whereas the dipole matrix $D^{nn'}$ only couples envelope functions of opposite parities. Third, the intersubband transitions for n-type quantum wells are forbidden except for light with a z polarization, whereas x, y, and z polarizations are allowed for p-type quantum wells. This feature makes p-type quantum wells more favorable than n-type quantum wells in most applications involving intersubband transitions, since it is much easier to send a light beam along the growth direction with an x (or y) polarization than along the in-plane direction with an x (or y) polarization.

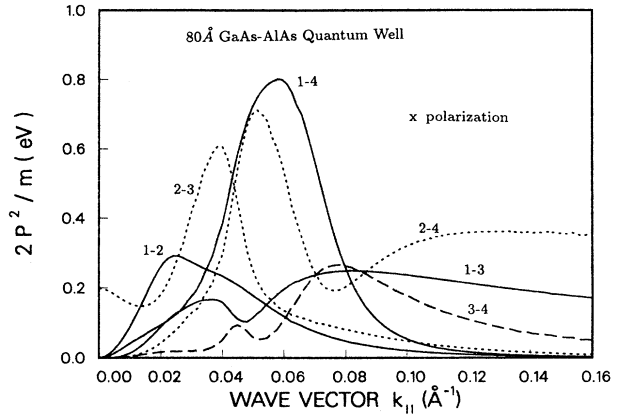

FIG. 2. Squared momentum matrix elements for an 80-Å GaAs-AlAs quantum well and light polarized along the x direction.

Figures 2 and 3 show the squared momentum matrix elements $2|\hat{\boldsymbol{\epsilon}}\cdot\mathbf{P}_{nn'}|^2/m_0$ for an 80-Å GaAs-AlAs quantum well as functions of the wave vector for $\hat{\boldsymbol{\epsilon}}\|\hat{\mathbf{x}}$ and $\hat{\boldsymbol{\epsilon}}\|\hat{\mathbf{z}}$, respectively. The features discussed above are clearly shown in these figures. In both of these figures we see a prominent transition labeled "1-4" (from the first subband to the fourth subband) which peaks around $k_\parallel=0.06$ Å^{-1}. Examining the subband structure of Fig. 1, we see that the energy separation between the first and fourth subbands matches the CO_2-laser energy (≈0.12 eV) at $k_\parallel\approx0.05$ Å^{-1}. Thus we expect the 1-4 transition at $k_\parallel\approx0.05$ Å^{-1} to play an important role in the absorption. We have also examined the squared matrix elements for 50- and 70-Å quantum wells and found qualitatively the same $k_\parallel$ dependence.

The average scattering rate is given by

$$\Gamma_{nn'}(\mathbf{k}_\parallel)=\tfrac{1}{2}\sum_{m,\mathbf{k}_\parallel'}(R_{n\mathbf{k}_\parallel\to m\mathbf{k}_\parallel'}+R_{n'\mathbf{k}_\parallel\to m\mathbf{k}_\parallel'})$$
$$\equiv\tfrac{1}{2}[\Gamma_n(\mathbf{k}_\parallel)+\Gamma_{n'}(\mathbf{k}_\parallel)] , \tag{9}$$

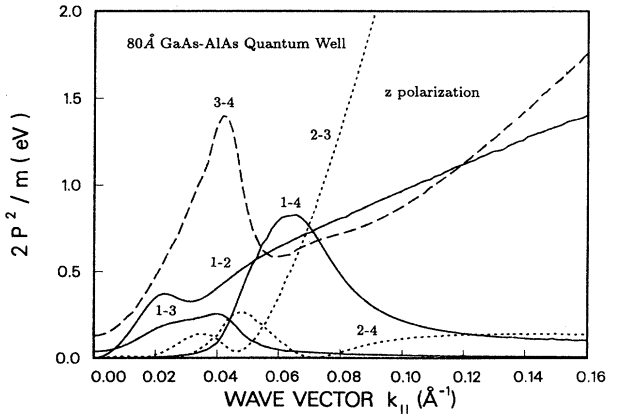

FIG. 3. Squared momentum matrix elements for an 80-Å GaAs-AlAs quantum well and light polarized along the z direction.

where $R_{n\mathbf{k}_\parallel \to m\mathbf{k}'_\parallel}$ is the rate at which a hole in subband state $|n,\mathbf{k}_\parallel\rangle$ is scattered into subband state $|m,\mathbf{k}'_\parallel\rangle$. In this paper we only include hole scattering from longitudinal-acoustical and longitudinal-optical (LO) phonons.

The scattering rate due to longitudinal-acoustical phonons is given by

$$R_{n\mathbf{k}_\parallel \to m\mathbf{k}'_\parallel}=\frac{2\pi}{\hbar}\sum_{\mathbf{q}}[|M^{+}_{\mathrm{ac}}(\mathbf{k}_\parallel,\mathbf{k}'_\parallel,\mathbf{q})|^2\delta_{\mathbf{k}'_\parallel,\mathbf{k}_\parallel+\mathbf{q}_\parallel}(N_{\mathbf{q}}+1)\delta(E_m(\mathbf{k}'_\parallel)-E_n(\mathbf{k}_\parallel)+\hbar\omega_{\mathbf{q}}) + |M^{-}_{\mathrm{ac}}(\mathbf{k}_\parallel,\mathbf{k}'_\parallel,\mathbf{q})|^2\delta_{\mathbf{k}'_\parallel,\mathbf{k}_\parallel-\mathbf{q}_\parallel}N_{\mathbf{q}}\delta(E_m(\mathbf{k}'_\parallel)-E_n(\mathbf{k}_\parallel)-\hbar\omega_{\mathbf{q}})] , \tag{10}$$

where

$$|M^{\pm}_{\mathrm{ac}}(\mathbf{k}_\parallel,\mathbf{k}'_\parallel,\mathbf{q})|^2=\frac{E^2_{\mathrm{ac}}q^2W}{2\rho V\omega_{\mathbf{q}}}\left|\sum_{\nu,\nu'}\int F^{*}_{\nu'}(m\mathbf{k}'_\parallel,z)e^{\pm iq_z z}F_{\nu}(n\mathbf{k}_\parallel,z)dz\right|^2$$

and $N_{\mathbf{q}}=(e^{\hbar\omega_{\mathbf{q}}/k_BT}-1)^{-1}$. ρ, V, and W are the mass density, volume of the crystal, and width of the quantum well, respectively. E_{ac} is the acoustical-phonon deformation potential. We have assumed the same deformation potential for HH-HH, HH-LH, and LH-LH scatterings. In this paper, we shall only consider the high-temperature regime ($T\geq 77$ K). Thus, $N_{\mathbf{q}}\approx k_BT/\hbar\omega_{\mathbf{q}} \gg 1$. We further assume the hole–acoustical-phonon scattering to be elastic, since the relevant acoustical phonons participating in the scattering process have energies small compared to the intersubband transition energies of interest. We then have

$$R_{n\mathbf{k}_\parallel \to m\mathbf{k}'_\parallel}=\frac{\pi E^2_{\mathrm{ac}}k_BT}{\hbar^2\rho Vc_l^2}G_{mn}\delta(E_n(\mathbf{k}_\parallel)-E_m(\mathbf{k}'_\parallel)) , \tag{11}$$

where c_l is the sound velocity of longitudinal phonons, and

$$G_{mn}=W\sum_{q_z}\left|\int dz\sum_{\nu,\nu'}F^{*}_{\nu'}(m\mathbf{k}'_\parallel,z)e^{\pm iq_z z}F_{\nu}(n\mathbf{k}_\parallel,z)\right|^2 = W\int dz\left|\sum_{\nu'}F_{\nu'}(m\mathbf{k}'_\parallel,z)\right|^2\left|\sum_{\nu}F_{\nu}(n\mathbf{k}_\parallel,z)\right|^2 . \tag{12}$$

For ease in computation, we shall approximate G_{mn} by its value at $\mathbf{k}_\parallel=\mathbf{k}'_\parallel=0$, since it depends on $\mathbf{k}_\parallel$ and $\mathbf{k}'_\parallel$ only weakly. Finally, the hole–acoustical-phonon scattering rate is given by

$$\Gamma_n(\mathbf{k}_\parallel)=\frac{\pi E^2_{\mathrm{ac}}k_BT}{\hbar^2\rho Vc_l^2}\sum_m D_m(E_n(\mathbf{k}_\parallel))G_{mn} , \tag{13}$$

where $D_m(E)\equiv\sum_{\mathbf{k}_\parallel}\delta(E-E_m(\mathbf{k}_\parallel))$ is the density of states associated with valence subband m.

The scattering rate due to longitudinal-optical phonons is similarly given by (10) with qE_{ac} replaced by D_0, the LO-phonon deformation-potential constant. The phonon frequencies $\omega_{\mathbf{q}}$ are replaced by the zone-center LO-phonon frequency ω_0, and $N_{\mathbf{q}}$ by $N_0\equiv(e^{\hbar\omega_0/k_BT}-1)^{-1}$. Thus, for the hole–optical-phonon scattering, we have

$$R_{n\mathbf{k}_\parallel \to m\mathbf{k}'_\parallel}=\frac{\pi D^2_0}{\hbar\rho V\omega_0}[(N_0+1)\delta(E_m(\mathbf{k}'_\parallel)-E_n(\mathbf{k}_\parallel)+\hbar\omega_0) + N_0\delta(E_m(\mathbf{k}'_\parallel)-E_n(\mathbf{k}_\parallel)-\hbar\omega_0)]G_{mn} \tag{14}$$

and

$$\Gamma_n(\mathbf{k}_\parallel)=\frac{\pi D^2_0}{\hbar\rho V\omega_0}\sum_m[D_m(E_n(\mathbf{k}_\parallel)-\hbar\omega_0)(N_0+1) + D_m(E_n(\mathbf{k}_\parallel)+\hbar\omega_0)N_0]G_{mn} . \tag{15}$$

It is easy to see that for each subband n the scattering rate depends on $\mathbf{k}_\parallel$ only via the subband energy $E_n(\mathbf{k}_\parallel)$. Namely, $\Gamma_n(\mathbf{k}_\parallel)=\Gamma_n(E_n(\mathbf{k}_\parallel))$. Figures 4 and 5 show the scattering rates $\Gamma_n(E)$ as functions of the subband energy E for an 80-Å GaAs-AlAs quantum well at 300 and 77 K, respectively. Also included in these figures for compar-

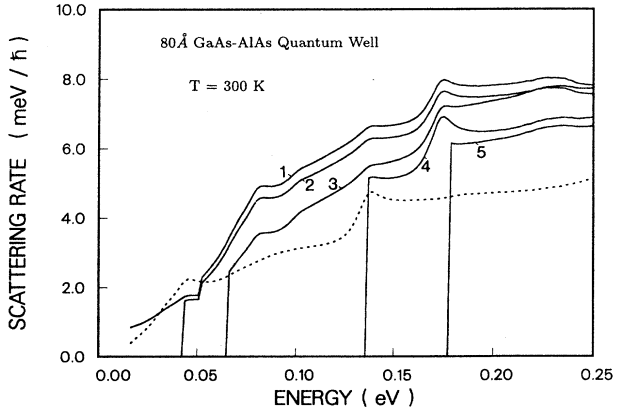

FIG. 4. Scattering rate and density of states of an 80-Å GaAs-AlAs quantum well as functions of the subband energy at $T=300$ K.

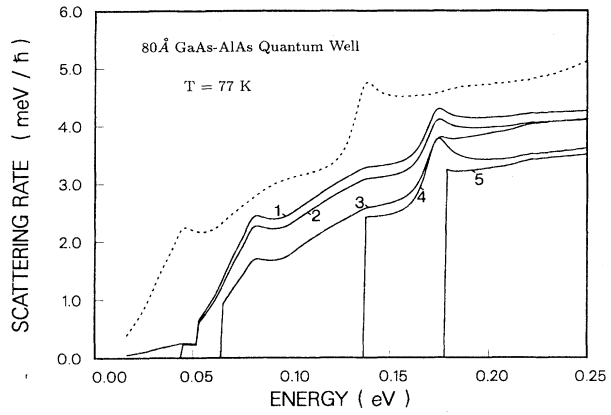

FIG. 5. Scattering rate and density of states of an 80-Å GaAs-AlAs quantum well as functions of the subband energy at $T=77$ K.

ison is the corresponding valence-band density of states (in arbitrary units). The scattering rate at 77 K is roughly one-half of that at 300 K. This is because the dominant scattering mechanism at 77 K is via the emission of an optical phonon, whereas at 300 K the other mechanisms are of comparable importance. We see that at 77 K the scattering rate as a function of energy resembles the density of states shifted to the high-energy side by the energy of an optical phonon, indicating the predominance of the emission of an optical phonon in the hole scattering. For states with energies less than an optical-phonon energy above the ground state ($E_0+\hbar\omega_0$), the scattering rate is very small, since it is not energetically possible to emit an optical phonon. Thus a discontinuous jump appears in the plots at $E_0+\hbar\omega_0$. Scattering rates associated with different subbands at a given energy only differ slightly via the factor G_{mn}.

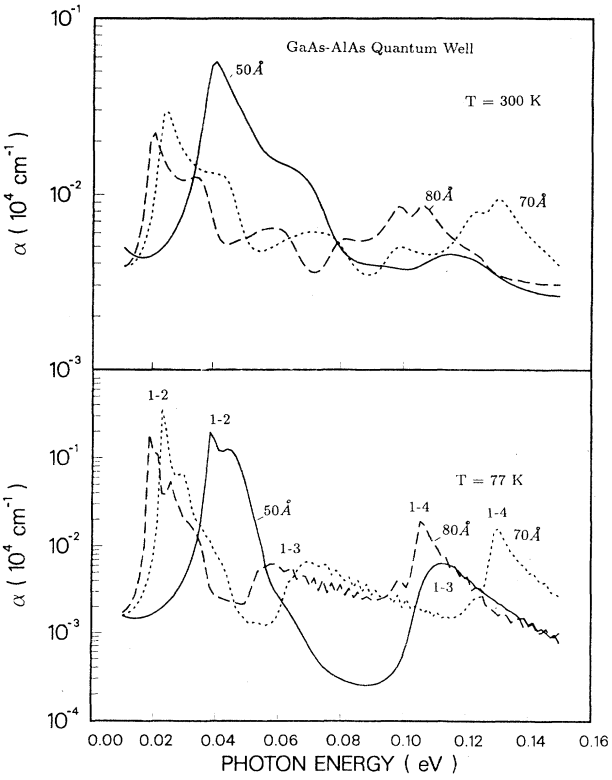

FIG. 6. Absorption spectra of three GaAs-AlAs quantum wells with well widths of 50, 70, and 80 Å at $T=300$ and 77 K. The doping concentration is 10^{12} cm^{-2}.

Figure 6 shows the absorption spectra of three GaAs-AlAs quantum wells with well widths 50, 70, and 80 Å at 300 and 77 K. The electric field of the incident radiation is parallel to the x direction. We find a large enhancement of the absorption coefficient (α) at the low-energy side, because the expression for α contains a prefactor which is inversely proportional to the photon energy [see (4)]. The predominant transitions responsible for the structures shown in the 77-K spectra are labeled. For photon energies that can be easily generated with a CO_2 laser (i.e., 114–134 meV), the absorption is dominated by the 1-4 transition for the 70- and 80-Å quantum wells and by the 1-3 transition for the 50-Å quantum well. In the 80-Å case, the energy difference between the first and fourth subbands ranges from 0.1 to 0.12 eV for wave vectors from 0 to 0.06 Å^{-1}, where both the carrier distribution and the optical matrix elements are appreciable (see Figs. 1 and 2). Thus, the absorption spectrum has a peak at $\hbar\omega\approx 0.1$ eV.

III. SATURATION OF INTERVALENCE-BAND TRANSITIONS

At low input-light intensities, the carrier distribution is approximately given by the equilibrium distribution $f_n^e(\mathbf{k}_\parallel)$, and Eq. (4) simply gives the linear absorption coefficient. At high input-light intensities, the optical transitions deplete the population of initially filled states so fast that the electron-phonon scattering cannot maintain the equilibrium distribution of carriers. The nonequilibrium distribution $f_n(\mathbf{k}_\parallel)$ is calculated by solving the rate equations[9]

$$\frac{\partial f_n(\mathbf{k}_\parallel)}{\partial t} = -\sum_m \beta_{nm}(\mathbf{k}_\parallel)[f_n(\mathbf{k}_\parallel)-f_m(\mathbf{k}_\parallel)] - \Gamma_n(\mathbf{k}_\parallel)f_n(\mathbf{k}_\parallel)+\sum_{m,\mathbf{k}'_\parallel} R_{m\mathbf{k}'_\parallel\to n\mathbf{k}_\parallel} f_m(\mathbf{k}'_\parallel)\ , \quad (16)$$

where

$$\beta_{nm}(\mathbf{k}_\parallel)\equiv \frac{2\pi^2 e^2 I}{(\epsilon_1)^{1/2} m_0^2 \hbar\omega^2 c}|\hat{\boldsymbol{\varepsilon}}\cdot\mathbf{P}_{nm}(\mathbf{k}_\parallel)|^2 \times \frac{\hbar\Gamma_{nm}(\mathbf{k}_\parallel)/\pi}{[\Delta_{nm}(\mathbf{k}_\parallel)-\hbar\omega]^2+[\hbar\Gamma_{nm}(\mathbf{k}_\parallel)]^2}\ . \quad (17)$$

Here I is the input-light intensity. The first term on the right-hand side represents the optical-depumping rate with carriers being photoexcited from subband n to all other subbands m, the second term represents the scatter-

ing rate of holes in subband n, and the third term represents the feeding rate with carriers being scattering into the subband n from all other subbands m. Note that at zero input-light intensity the equilibrium distribution $f_n^e(\mathbf{k}_\parallel)$ satisfies the rate equations

$$\Gamma_n(\mathbf{k}_\parallel)f_n^e(\mathbf{k}_\parallel)-\sum_{m,\mathbf{k}'_\parallel} R_{m\mathbf{k}'_\parallel\to n\mathbf{k}_\parallel} f_m^e(\mathbf{k}'_\parallel)=0 \ . \tag{18}$$

Subtracting (18) from (16), we immediately obtain

$$\frac{\partial g_n(\mathbf{k}_\parallel)}{\partial t} = B_n(\mathbf{k}_\parallel)-\sum_m \beta_{nm}(\mathbf{k}_\parallel)[g_n(\mathbf{k}_\parallel)-g_m(\mathbf{k}_\parallel)] -\Gamma_n(\mathbf{k}_\parallel)g_n(\mathbf{k}_\parallel)+\sum_{m,\mathbf{k}'_\parallel} R_{m\mathbf{k}'_\parallel\to n\mathbf{k}_\parallel} g_m(\mathbf{k}'_\parallel) \ , \tag{19}$$

where we have defined

$$g_n(\mathbf{k}_\parallel)\equiv f_n(\mathbf{k}_\parallel)-f_n^e(\mathbf{k}_\parallel) \tag{20}$$

and

$$B_n(\mathbf{k}_\parallel)=-\sum_m \beta_{nm}(\mathbf{k}_\parallel)[f_n^e(\mathbf{k}_\parallel)-f_m^e(\mathbf{k}_\parallel)] \ . \tag{21}$$

To solve for the nonequilibrium distribution $f_n(\mathbf{k}_\parallel)$, we assume that the light intensity is turned on suddenly at $t=0$, viz.,

$$I(t)=I\Theta(t) \ ,$$

where $\Theta(t)$ is a step function. We use an iterative method to calculate $g_n(\mathbf{k}_\parallel)$ as a function of t subject to the initial condition $g_n(\mathbf{k}_\parallel)=0$. We divide the time interval $(0,t)$ into N (a large number) short-time intervals $(s\tau,(s+1)\tau)$, $s=0,1,\ldots,N-1$. Here, $\tau=t/N$. The function $g_n(\mathbf{k}_\parallel)$ at time $s\tau$ is denoted by $g_n^{(s)}(\mathbf{k}_\parallel)$. Since τ is sufficiently small, we have

$$[g_n^{(s+1)}(\mathbf{k}_\parallel)-g_n^{(s)}(\mathbf{k}_\parallel)]/\tau\approx B_n(\mathbf{k}_\parallel)-\sum_m \beta_{nm}(\mathbf{k}_\parallel)[g_n^{(s)}(\mathbf{k}_\parallel)-g_m^{(s)}(\mathbf{k}_\parallel)]-\Gamma_n(\mathbf{k}_\parallel)g_n^{(s)}(\mathbf{k}_\parallel)+\sum_{m,\mathbf{k}'_\parallel} R_{m\mathbf{k}'_\parallel\to n\mathbf{k}_\parallel} g_m^{(s)}(\mathbf{k}'_\parallel) \ .$$

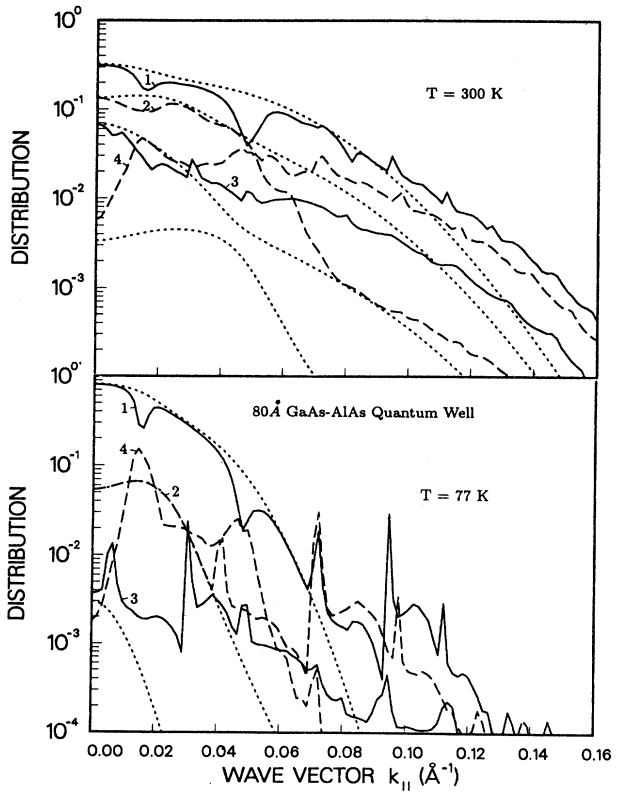

FIG. 7. Distribution functions for various valence subbands of an 80-Å GaAs-AlAs quantum well for incident radiation at $\hbar\omega=0.117$ meV and $I=50$ MW/cm^2 at $T=300$ and 77 K. Solid and dashed curves, steady-state intensity-dependent distribution; dotted curves, equilibrium distribution.

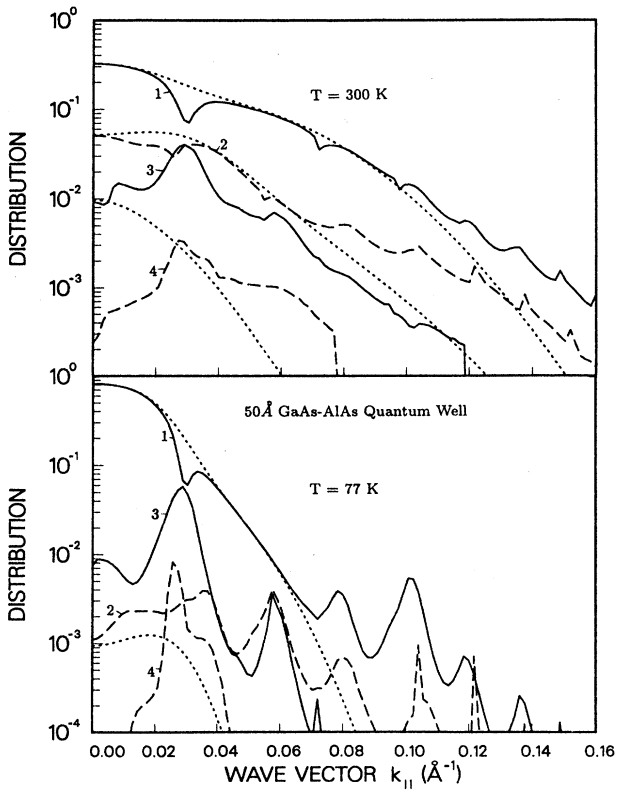

FIG. 8. Distribution functions for various valence subbands of a 50-Å GaAs-AlAs quantum well under optical pumping at $\hbar\omega=0.117$ meV and $I=50$ MW/cm^2 at $T=300$ and 77 K. Solid and dashed curves, steady-state intensity-dependent distribution; dotted curves, equilibrium distribution.

The above recursion relation was used to solve $g_n(\mathbf{k}_\parallel)$ [and thus $f_n(\mathbf{k}_\parallel)$] at any time t. For sufficiently large time t, we obtain a steady-state solution.

To make the computation tractable, we have ignored the anisotropy in the valence-subband structure. For each subband n we select a set of mesh points of $k_\parallel$ whose corresponding energies $E_n(k_\parallel)$ are evenly spaced, and the optical-phonon energy $\hbar\omega_0$ is an integral multiple of the energy spacing of two consecutive mesh points. This selection is necessary as the scattering matrix $R_{n\mathbf{k}_\parallel \to m\mathbf{k}'_\parallel}$ only links states which differ by integral multiples of $\hbar\omega_0$.

Figure 7 shows the distribution functions (solid and dashed curves) for various valence subbands of an 80-Å GaAs-AlAs quantum well at 300 and 77 K for a pump beam with $\hbar\omega=0.117$ eV and $I=50$ MW/cm^2. Also included for comparison are the corresponding equilibrium distribution functions (dotted curves). The electric field of the incident radiation is parallel to the x direction. In the semilogarithmic graph, the equilibrium distributions as a function of $\mathbf{k}_\parallel$ resemble the subband structure, because in the nondegenerate regime the carrier distribution is proportional to the Boltzmann factor. For the first subband, carriers are partially depleted (due to optical depumping) at wave vectors near 0.018 and 0.05 Å^{-1}, and backfilled (due to carrier-phonon scattering) at larger wave vectors. The largest depletion occurs at $k_\parallel \approx 0.05$ Å^{-1}, where the energy for the 1-4 transition matches the energy of the pump beam [see Fig. 1(b)]. Because the optical matrix elements are strong for the 1-4 transition at $k_\parallel \approx 0.05$ Å^{-1} (see Fig. 2), the carrier distribution in the fourth subband at $k_\parallel \approx 0.05$ Å^{-1} is substantially increased, giving rise to a peaked structure. The behavior at $k_\parallel \approx 0.018$ Å^{-1} is similar, but to a lesser degree. The other structures seen in the figure, which appear at subband energies separated by integral multiples of the optical-phonon energy are due to carrier–optical-phonon scatterings. The corresponding carrier distributions for the 50-Å case are shown in Fig. 8. The behavior can again be understood by examining the subband structures and the optical matrix elements.

Figure 9 shows the intensity dependence of the nonlinear absorption coefficient $\alpha(I)$, normalized to the linear absorption coefficient α_0, of the 80-Å quantum well for incident photon energies of 0.11, 0.117, and 0.14 eV at 300 and 77 K, respectively. The electric field of the incident radiation is parallel to the x direction. We find that the saturation curve can be approximated by an inhomogeneously broadened two-level model, i.e., $\alpha(I)/\alpha_0 \approx (1+I/I_s)^{-1/2}$, where I_s is the saturation intensity. The saturation intensity can be determined by finding the value of I at which $\alpha(I)/\alpha_0=0.707$. From this figure, we find that the saturation intensity ranges from 1 to 3 MW/cm^2 at 77 K and from 5 to 10 MW/cm^2 at 300 K. This represents some (although not substantial) improvement over bulk GaAs, which has a saturation intensity of 15 MW/cm^2 at 300 K.[18] Figure 10 shows the similar $[\alpha(I)/\alpha_0]$-versus-I plots for a 70-Å quantum well. The saturation intensities ranges from 8 to 12 MW/cm^2 at 77 K and from 7 to 17 MW/cm^2 at 300 K. The large difference in saturation intensity for the 70- and 80-Å cases is caused by the difference in subband structures. As shown in Figs. 5 and 6, the different subband structures lead to different peak positions in the absorption spectra (0.105 eV for the 80-Å case and 0.13 eV for the 70-Å case). Because of the asymmetric line shape of the absorption peak, I_s is smaller and less sensitive to $\hbar\omega$

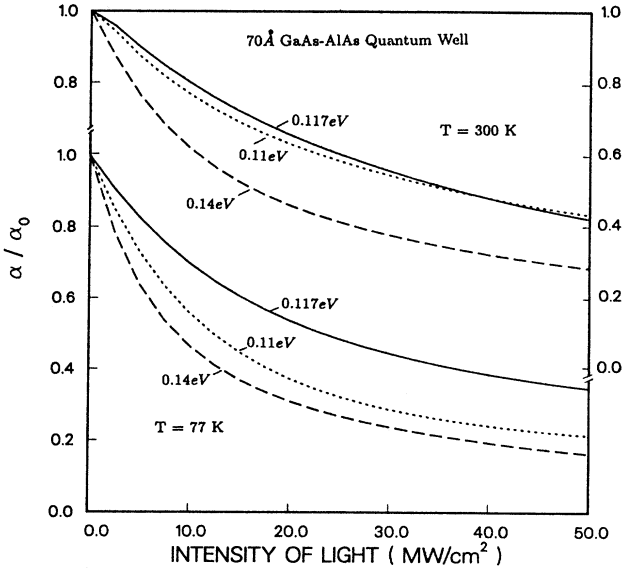

FIG. 9. $\alpha(I)/\alpha_0$ of an 80-Å GaAs-AlAs quantum well as functions of I for incident radiation at $\hbar\omega=0.11$, 0.117, and 0.14 eV at $T=300$ and 77 K. The values of $\alpha(I)/\alpha_0$ are shown on the right-hand (left-hand) side at 300 K (77 K).

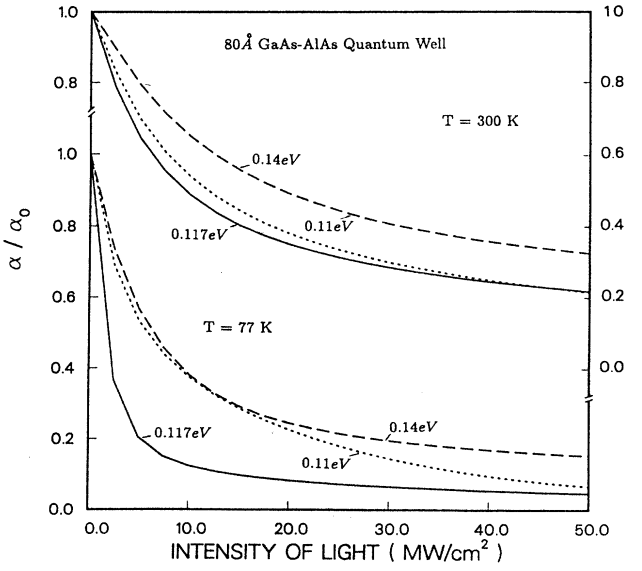

FIG. 10. $\alpha(I)/\alpha_0$ of a 70-Å GaAs-AlAs quantum well as functions of I for incident radiation at $\hbar\omega=0.11$, 0.117, and 0.14 eV at $T=300$ and 77 K. The values of $\alpha(I)/\alpha_0$ are shown on the right-hand (left-hand) side at 300 K (77 K).

when $\hbar\omega$ is slightly higher than the peak position (e.g., the 80-Å case with $\hbar\omega=0.11-0.14$ eV), and I_s becomes substantially larger when $\hbar\omega$ is slightly lower than the peak position (e.g., the 70-Å case at $\hbar\omega=0.117$ eV). For the 50-Å quantum well (not shown), we found that the saturation intensities range from 7 to 8 MW/cm^2 at 77 K and from 10 to 15 MW/cm^2 at 300 K.

IV. PHOTOABSORPTION IN THE PRESENCE OF A PUMP BEAM

Another possible application of the intersubband absorption saturation in p-type semiconductor quantum wells is a light-by-light modulator.[19,20] Because of the rich structures in the valence subbands in quantum wells, there are many ways of modifying the absorption spectrum of a weak probe beam by an intense pump beam. The intense pump beam causes a steady-state carrier distribution which is different from the equilibrium distribution. Since the direct free-hole transitions between different subbands are linked by population-bleaching effects, the absorption spectrum of a probe beam will be altered by the presence of a pump beam, and the amount of change in the probe absorption can be controlled by tuning the wavelength and intensity of the pump beam. The modulation time constant for the probe absorption is determined by the population relaxation time, which is less than 1 ps for a pump beam having a wavelength near 10 μm. The experimental observation of such frequency correspondences can also be used to measure the energy separations between the valence subbands, similar to the approach utilized in Ref. 18 to test the valence-subband structure of germanium.

To the first-order approximation, the absorption coefficient for the probe beam is described by (4) with the carrier distribution determined by solving (16) for the pump beam. Figures 11 and 12 show the probe absorption spectra of 80- and 50-Å GaAs-AlAs quantum wells with and without a 50-MW/cm^2 pump beam at $\hbar\omega=0.117$ meV. The electric fields for both the pump-and-probe beams are taken to be along the x direction. For the 50-Å quantum well at 77 K, we found a negative absorption coefficient for $\hbar\omega\approx0.07-0.09$ eV, indicating a gain. In the semilogarithmic plot, we show the absolute value of α with the understanding that the sign of α is negative for photon energies in the range of about 0.07–0.09 eV. For all cases shown in Figs. 11 and 12, the absorption coefficient is substantially reduced for $\hbar\omega$ near the pump frequency as a result of carrier depletion. The change of absorption at other photon energies reflects the nonequilibrium carrier distribution set up by the pump beam. The absorption coefficient is reduced to various

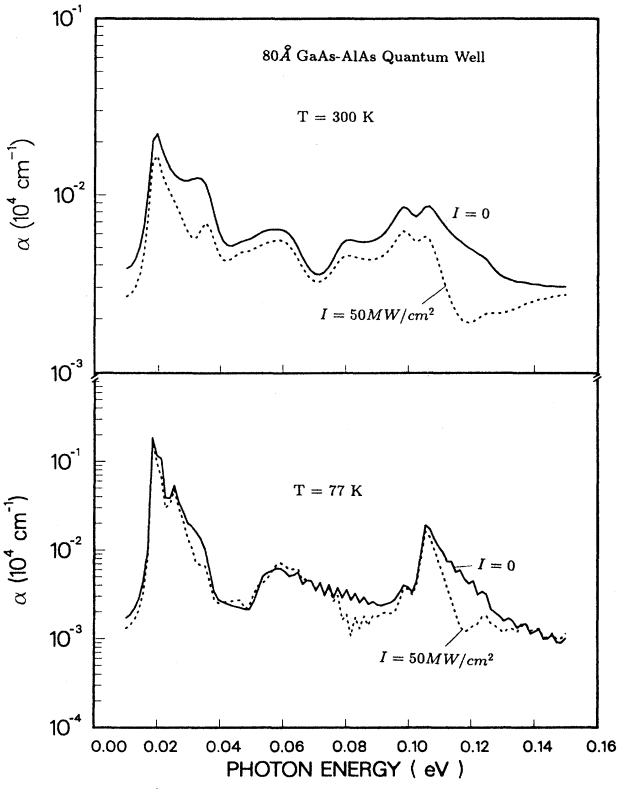

FIG. 11. Absorption spectra of an 80-Å GaAs-AlAs quantum well under optical pumping at $\hbar\omega=0.117$ meV and $I=50$ MW/cm^2 at $T=300$ and 77 K. The doping concentration is 10^{12} cm^{-2}.

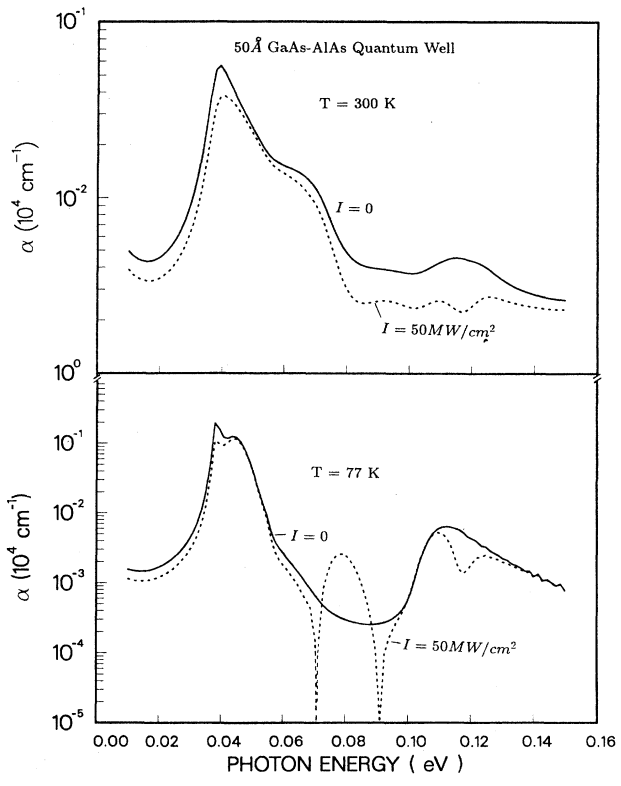

FIG. 12. Absorption spectra of a 50-Å GaAs-AlAs quantum well under optical pumping at $\hbar\omega=0.117$ meV and $I=50$ MW/cm^2 at $T=300$ and 77 K. The doping concentration is 10^{12} cm^{-2}.

degrees at almost all photon energies shown in these figures. This is because the absorption at these energies is dominated by optical transitions from the low-energy states in which the carriers are partially depleted. At higher photon energies, where the optical transitions from states with energies higher than $E_0+0.117$ eV (E_0 being the ground-state hole energy) become important, we would expect an increase in the absorption coefficient due to the increased population of these high-energy states by the pump beam. The appearance of the gain for the 50-Å case is due to the inverted population of the third subband relative to the second subband at $k_{\|}$ near 0.03 $Å^{-1}$ (see Fig. 6) and the sizable 2-3 transition at that wave vector (see Fig. 2). Note that the dependence of the optical matrix elements on $k_{\|}$ is not sensitive to the variation of the quantum-well width. The peak position of the gain is around 0.08 eV, which agrees well with the energy separation of subbands 2 and 3 at $k_{\|}\approx 0.03$ $Å^{-1}$ [see Fig. 1(a)]. By sweeping the frequency of the pump beam and measuring the probe absorption spectrum, one can map out the energy difference of various subbands as a function of $\mathbf{k}_{\|}$, thus obtaining valuable information about the valence-band structures of quantum wells.

V. SUMMARY AND CONCLUSIONS

We have studied the absorption coefficients associated with intersubband transitions and their saturation behavior in p-type GaAs-AlAs quantum wells. We found that the p-type quantum wells are more accessible experimentally than n-type quantum wells, because in the former case the intersubband absorption is appreciable for incident light propagating along the growth direction (the desired experimental setup). We found prominent structures in the absorption spectra corresponding to various subband-to-subband transitions. The peak absorption near the CO_2-laser frequencies are around a few hundred cm^{-1} for a free-hole concentration of 10^{12} cm^{-2}. The saturation intensity I_s is smallest for quantum-well widths around 80 Å and I_s is around 1 MW/cm^2 at 77 K and 5 MW/cm^2 at 300 K at a photon energy of 0.117 eV. When the well width is not optimized, I_s is comparable to that of bulk GaAs. We have also studied the pump-and-probe absorption spectra. We found some relations between the absorption spectrum for the probe beam and the nonequilibrium carrier distributions set up by the pump beam. These relations can serve as a guide for designing light-by-light modulators and for pump-and-probe experiments for investigating band structures of p-type modulation-doped semiconductor quantum wells.

ACKNOWLEDGMENTS

We would like to thank D. L. Smith and M. I. Baskes for fruitful discussions. One of us (Y.C.C.) would like to thank Sandia National Laboratories, Livermore, CA, for its support. This work was supported in part by the U.S. Office of Naval Research (ONR) under Contract No. N00014-81-K-0430. One of us (R.B.J.) would like to acknowledge support from the U.S. Department of Energy.

APPENDIX: DERIVATION OF THE MOMENTUM MATRIX ELEMENTS

The momentum matrix element between quantum-well valence-subband states $|n,\mathbf{k}_{\|}\rangle$ and $|n',\mathbf{k}_{\|}\rangle$ is defined by

$$\frac{\hbar}{m_0}\hat{\boldsymbol{\varepsilon}}\cdot\mathbf{P}_{nn'}=\left\langle n,\mathbf{k}_{\|}\left|\frac{\hbar}{m_0}\hat{\boldsymbol{\varepsilon}}\cdot\mathbf{p}\right|n',\mathbf{k}_{\|}\right\rangle . \tag{A1}$$

Using the expansion $|n,\mathbf{k}_{\|}\rangle=\sum_{\nu,\mathbf{k}_z}F_\nu(n\mathbf{k}_{\|},k_z)|\nu,\mathbf{k}\rangle$ as given in (2), we have

$$\frac{\hbar}{m_0}\hat{\boldsymbol{\varepsilon}}\cdot\mathbf{P}_{nn'}=\sum_{\nu,\nu',k_z}F_\nu^*(n\mathbf{k}_{\|},k_z)F_{\nu'}(n\mathbf{k}_{\|},k_z)\left\langle\nu,\mathbf{k}\left|\frac{\hbar}{m_0}\hat{\boldsymbol{\varepsilon}}\cdot\mathbf{p}\right|\nu',\mathbf{k}\right\rangle , \tag{A2}$$

where $|\nu,\mathbf{k}\rangle$ is given by (1). Note that in $\mathbf{k}\cdot\mathbf{p}$ theory,[16] the 4×4 Luttinger-Kohn Hamiltonian for semiconductors with large spin-orbit splitting can be written as

$$\begin{aligned}H^{(0)}_{\nu\nu'}(\mathbf{k})&\equiv\langle u_{3/2,\nu}|H^{(0)}-E_0|\nu',\mathbf{k}\rangle\\&=\frac{\hbar^2k^2}{2m_0}\delta_{\nu\nu'}+\frac{\hbar^2}{m_0^2}\sum_s\frac{\langle u_{3/2,\nu}|\mathbf{k}\cdot\mathbf{p}|u_s\rangle\langle u_s|\mathbf{k}\cdot\mathbf{p}|u_{3/2,\nu'}\rangle}{E_0-E_s}\\&\equiv\sum_{i,j}D^{ij}_{\nu\nu'}k_ik_j ,\end{aligned} \tag{A3}$$

where $H^{(0)}$ is the bulk Hamiltonian, E_0 is the energy of the valence-band maximum, and $D^{ij}_{\nu\nu'}$ are the coefficients for the valence-band effective-mass tensor. Therefore, we have

$$\begin{aligned}\frac{\hbar}{m_0}\langle\nu,\mathbf{k}|\hat{\boldsymbol{\varepsilon}}\cdot\mathbf{p}|\nu',\mathbf{k}\rangle&=\frac{\hbar^2}{m_0}\hat{\boldsymbol{\varepsilon}}\cdot\mathbf{k}\delta_{\nu\nu'}+\frac{\hbar^2}{m_0^2}\sum_s\frac{\langle u_{3/2,\nu}|\hat{\boldsymbol{\varepsilon}}\cdot\mathbf{p}|u_s\rangle\langle u_s|\mathbf{k}\cdot\mathbf{p}|u_{3/2,\nu'}\rangle+\langle u_{3/2,\nu}|\mathbf{k}\cdot\mathbf{p}|u_s\rangle\langle u_s|\hat{\boldsymbol{\varepsilon}}\cdot\mathbf{p}|u_{3/2,\nu'}\rangle}{E_0-E_s}\\&=\sum_{i,j}(D^{ij}_{\nu\nu'}+D^{ji}_{\nu\nu'})\epsilon_ik_j .\end{aligned} \tag{A4}$$

Separating terms in (A3) that are proportional to k_z from the rest and substituting (A3) into (A2), we obtain

$$\hat{\varepsilon}\cdot\mathbf{P}_{nn'}=\hbar\hat{\varepsilon}\cdot\sum_{\nu,\nu'}(\mathbf{P}_{\nu\nu'}O_{\nu\nu'}^{nn'}+\mathbf{Q}_{\nu\nu'}D_{\nu\nu'}^{nn'}) , \tag{A5}$$

where

$$\hat{\varepsilon}\cdot\mathbf{P}_{\nu\nu'}\equiv\sum_i \epsilon_i[(D_{\nu\nu'}^{xi}+D_{\nu\nu'}^{ix})k_x+(D_{\nu\nu'}^{yi}+D_{\nu\nu'}^{iy})k_y] ,$$

$$\hat{\varepsilon}\cdot\mathbf{Q}_{\nu\nu'}\equiv\sum_i \epsilon_i(D_{\nu\nu'}^{zi}+D_{\nu\nu'}^{iz}) ,$$

$$O_{\nu\nu'}^{nn'}\equiv\sum_{k_z} F_\nu^*(n\mathbf{k}_\parallel,k_z)F_{\nu'}(n\mathbf{k}_\parallel,k_z)=\int dz\, F_\nu^*(n\mathbf{k}_\parallel,z)F_{\nu'}(n\mathbf{k}_\parallel,z) ,$$

$$D_{\nu\nu'}^{nn'}\equiv\sum_{k_z} F_\nu^*(n\mathbf{k}_\parallel,k_z)k_zF_{\nu'}(n\mathbf{k}_\parallel,k_z)=\int dz\, F_\nu^*(n\mathbf{k}_\parallel,z)\left[-i\frac{\partial}{\partial z}\right]F_{\nu'}(n\mathbf{k}_\parallel,z) .$$

Explicit expressions of $\hat{\varepsilon}\cdot\mathbf{P}_{\nu\nu'}$ and $\hat{\varepsilon}\cdot\mathbf{Q}_{\nu\nu'}$ are given in Table I.

[1]E. O. Kane, J. Phys. Chem. Solids **1**, 82 (1956).
[2]M. Zaluzny, Thin Solid Films **76**, 307 (1981).
[3]D. Ahn and S. L. Chuang, J. Appl. Phys. **62**, 3052 (1987).
[4]Y. C. Chang and J. N. Schulman, Appl. Phys. Lett. **43**, 536 (1983); Phys. Rev. B **31**, 2069 (1985).
[5]M. Altarelli, Phys. Rev. B **32**, 5138 (1985).
[6]G. D. Sanders and Y. C. Chang, Phys. Rev. B **31**, 6892 (1985); **36**, 4849 (1987).
[7]R. C. Miller, A. C. Gossard, G. D. Sanders, Y. C. Chang, and J. N. Schulman, Phys. Rev. B **32**, 8452 (1985).
[8]A. F. Gibson, C. A. Rosito, C. A. Raffo, and M. F. Kimmitt, Appl. Phys. Lett. **21**, 356 (1972).
[9]R. B. James and D. L. Smith, Phys. Rev. Lett. **42**, 1495 (1979); Phys. Rev. B **21**, 3502 (1980).
[10]A. J. Alcock and A. C. Walker, Appl. Phys. Lett. **25**, 299 (1974).
[11]B. J. Feldman and J. F. Figueria, Appl. Phys. Lett. **25**, 301 (1974).
[12]A. F. Gibson, M. F. Kimmitt, and B. Norris, Appl. Phys. Lett. **24**, 306 (1974).
[13]D. A. B. Miller, D. S. Chemla, T. C. Damen, A. C. Gossard, W. Wiegman, T. H. Wood, and C. A. Burrus, Appl. Phys. Lett. **45**, 13 (1984).
[14]W. L. Bloss and L. Friedman, Appl. Phys. Lett. **41**, 1023 (1982).
[15]Y. C. Chang, Appl. Phys. Lett. **40**, 710 (1985); J. Appl. Phys. **58**, 499 (1985).
[16]J. M. Luttinger and W. Kohn, Phys. Rev. **97**, 869 (1955).
[17]D. J. Wolford, T. F. Keuch, J. A. Bradley, M. A. Gell, D. Ninno, and M. Jaros, J. Vac. Sci. Technol. B **4**, 1043 (1986).
[18]F. Keilmann, Solid State Commun. **25**, 451 (1978).
[19]E. Conwell, J. Phys. Chem. Solids **8**, 236 (1959).
[20]R. B. James, W. H. Christie, R. E. Eby, B. E. Mills, and L. S. Darken, Jr., J. Appl. Phys. **59**, 1323 (1986).